Applied Physics Letters ARTICLE scitation.org/journal/apl

Distributed polarization-doped GaN p–n diodes with near-unity ideality factor and avalanche breakdown voltage of 1.25 kV

Cite as: Appl. Phys. Lett. **120**, 122111 (2022); doi: 10.1063/5.0083302
Submitted: 23 December 2021 · Accepted: 23 February 2022 ·
Published Online: 24 March 2022

Kazuki Nomoto,[1] Wenshen Li,[1,a)] Bo Song,[1] Zongyang Hu,[1] Mingda Zhu,[1] Meng Qi,[2] Vladimir Protasenko,[1] Zexuan Zhang,[1] Ming Pan,[3] Xiang Gao,[3] Hugues Marchand,[3] Wayne Johnson,[3] Debdeep Jena,[1,4,5] and Huili Grace Xing[1,4,5,a)]

AFFILIATIONS

[1]School of Electrical and Computer Engineering, Cornell University, Ithaca, New York 14853, USA
[2]Department of Electrical Engineering, University of Notre Dame, Notre Dame, Indiana 46556, USA
[3]IQE, Somerset, New Jersey 08873, USA
[4]Department of Materials Science and Engineering, Cornell University, Ithaca, New York 14853, USA
[5]Kavli Institute at Cornell for Nanoscale Science, Cornell University, Ithaca, New York 14853, USA

Note: This paper is part of the APL Special Collection on Wide- and Ultrawide-Bandgap Electronic Semiconductor Devices.
[a)]**Authors to whom correspondence should be addressed:** wl552@cornell.edu and grace.xing@cornell.edu

ABSTRACT

Polarization-induced (Pi) distributed or bulk doping in GaN, with a zero dopant ionization energy, can reduce temperature or frequency dispersions in impurity-doped p–n junctions caused by the deep-acceptor-nature of Mg, thus offering GaN power devices promising prospects. Before comprehensively assessing the benefits of Pi-doping, ideal junction behaviors and high-voltage capabilities should be confirmed. In this work, we demonstrate near-ideal forward and reverse *I–V* characteristics in Pi-doped GaN power p–n diodes, which incorporates linearly graded, coherently strained AlGaN layers. Hall measurements show a net increase in the hole concentration of 8.9×10^{16} cm^{-3} in the p-layer as a result of the polarization charge. In the Pi-doped n-layer, a record-low electron concentration of 2.5×10^{16} cm^{-3} is realized due to the gradual grading of $Al_{0\text{-}0.72}GaN$ over 1 μm. The Pi-doped p–n diodes have an ideality factor as low as 1.1 and a 0.10 V higher turn-on voltage than the impurity-doped p–n diodes due to the increase in the bandgap at the junction edge. A differential specific on-resistance of 0.1 mΩ cm^2 is extracted from the Pi-doped p–n diodes, similar with the impurity-doped counterpart. The Pi-doped diodes show an avalanche breakdown voltage of ~1.25 kV, indicating a high reverse blocking capability even without an ideal edge-termination. This work confirms that distributed Pi-doping can be incorporated in high-voltage GaN power devices to increase hole concentrations while maintaining excellent junction properties.

GaN-based electronic devices have marked excellent records for high-frequency, high-power, and high-efficiency applications.[1–6] A major underlying reason behind the success is the unique polarization-induced (Pi) doping scheme, which gives rise to a high-mobility two-dimensional electron gas (2DEG) without the need for impurity dopants.[7] Recently, a two-dimensional hole gas (2DHG) was also reported in undoped GaN/AlN structures.[8] In addition to the generation of two-dimensional carriers from a polarization discontinuity across a heterojunction interface, Pi-*bulk* or *distributed* doping for three-dimensional electron gas[9] and hole gas[10] with a constant bulk concentration can also be obtained from a constant polarization gradient in linearly graded structures.

Since the mobile carriers are induced electrostatically from the fixed polarization charge, the carriers from Pi-bulk doping will not freeze out at low temperatures,[9,10] i.e., the dopant activation energy is zero. This important feature not only allows for low-temperature wide-bandgap electronics, but can also eliminate the frequency dispersion caused by deep dopants, such as Mg in GaN.[11] Specifically, the cutoff frequency of charge response will no longer be limited by the emission rate of deep dopants,[12] but will reach the intrinsic limit imposed by the dielectric relaxation time.[13]

The unique advantages of Pi-bulk doping have important bearing on vertical GaN power devices in which p-type doping is widely used. With the availability of high-quality bulk GaN substrates in recent

years, high-voltage GaN power p–n diodes have been demonstrated since 2013,[14–25] including the first observation of simultaneous near-unity ideality factor and avalanche breakdown in 2015[17] and uniform avalanche breakdown in 2018.[24] In addition, various types of vertical GaN power transistors have been demonstrated.[26–31] Despite the promising progress, challenges related to Mg-doped p-layers still remain. First, buried p-GaN layers grown by metal-organic chemical vapor deposition (MOCVD) are difficult to activate, leading to additional constraints on the device design and fabrication process.[32,33] Second, the deep-acceptor nature of Mg causes frequency dispersion as mentioned previously, which may compromise the dynamic switching performance. Third, heavy-Mg doping required in the p-body due to the low doping efficiency leads to a low electron mobility in inversion MOS channels. With the incorporation of Pi-doping in the p-layer, these challenges could be mitigated. To this end, we have proposed and made an initial demonstration of a novel vertical power transistor called PolarMOS,[34,35] which features the Pi-bulk doping in the body p–n junction via graded AlGaN. We have shown that the presence of polarization charge in the buried p-layer increases the open-base punch-through voltage despite the presence of H, i.e., passivation of Mg.[36] Other benefits of the Pi-doped p-layer await further investigation.

As a core component in the PolarMOS, the Pi-doped body p–n junction requires detailed study and should exhibit ideal junction behaviors. In addition, a low-enough Pi-doping concentration ($<10^{17}\,cm^{-3}$) in the n-type drift layer is required for a high breakdown voltage (BV). Previously, Pi-doped p–n junctions have been reported,[10,37–39] but high-voltage (>500 V) capabilities have not been demonstrated. Recently, we reported over 1 kV breakdown voltage and avalanche capability in Pi-doped p–n diodes,[40,41] but the n-layer contains a high level of carbon as compensating centers.[41] As a result, the forward I–V characteristics and polarization charge in the n-side cannot be accurately assessed. To date, the lowest measured electron concentration in the Pi-doped graded AlGaN layer is $3.8\times10^{16}\,cm^{-3}$.[42] In this work, we report the realization of avalanche-capable Pi-doped GaN p–n diode with near-ideal forward and reverse I–V characteristics. An increase in the hole concentration in the p-layer due to Pi-doping is confirmed from Hall effect measurements. Through a 1-μm thick graded AlGaN layer, a record-low electron concentration of $2.5\times10^{16}\,cm^{-3}$ is realized in the Pi-doped n-layer.

As shown in Fig. 1(a), the epitaxial structure of the Pi-doped p–n diode consists of a 0.2-μm n^+-GaN (Si: $1\times10^{18}\,cm^{-3}$) buffer layer, a 7-μm impurity-doped n^--GaN (Si: $\sim2\times10^{16}\,cm^{-3}$) drift layer, a 1-$\mu$m Pi-doped Al_xGaN n^--GaN ($x=0\rightarrow7.2\%$) drift layer without Si-doping, a 450-nm Pi-doped Al_xGaN p-layer ($x=7.2\%\rightarrow0$) with an additional Mg doping concentration of $1\times10^{19}\,cm^{-3}$, and a 20-nm p^{++}-GaN capping layer for the anode Ohmic contact. The Mg doping was designed in the Pi-doped p-layer to minimize compensation due to point defects and to provide additional acceptors, since at the present stage the Pi-doping alone with a 7.2% peak Al concentration does not provide enough negative charge to prevent punch-through of the p-layer at avalanche breakdown. To study the influence of the Pi-doping, an impurity-doped p–n diode structure was designed as a control, as shown in Fig. 1(b). The only design difference is the absence of the Pi-doping, which is replaced by Si-doping in the drift layer. Both the pi-doped and impurity-doped samples were grown by MOCVD on 2-in. bulk n^+-GaN substrates (SCIOCS COMPANY Ltd.). The schematic cross sections of the fabricated circular p–n diodes are illustrated in Fig. 1. A beveled field plate was implemented as the edge termination. The detailed fabrication process of the diodes is described in our previous work.[15] The diode size is defined by the bottom diameter of the mesa to minimize over-estimation of the device performance since the effective current-carrying device area is larger than the anode metal contact area.[43]

Figure 2 shows secondary ion mass spectrometry (SIMS) analysis of the Pi-doped sample. The Al composition profile shows good linearity. The carbon concentration is reduced to be $\leq1\times10^{16}\,cm^{-3}$, which is much lower than the earlier generation.[41] This is enabled by an increase in the MOCVD temperature during the growth of the entire n-drift layer for the Pi-doped p–n junction, relative to that of the impurity-doped p–n junction. The increase in the growth

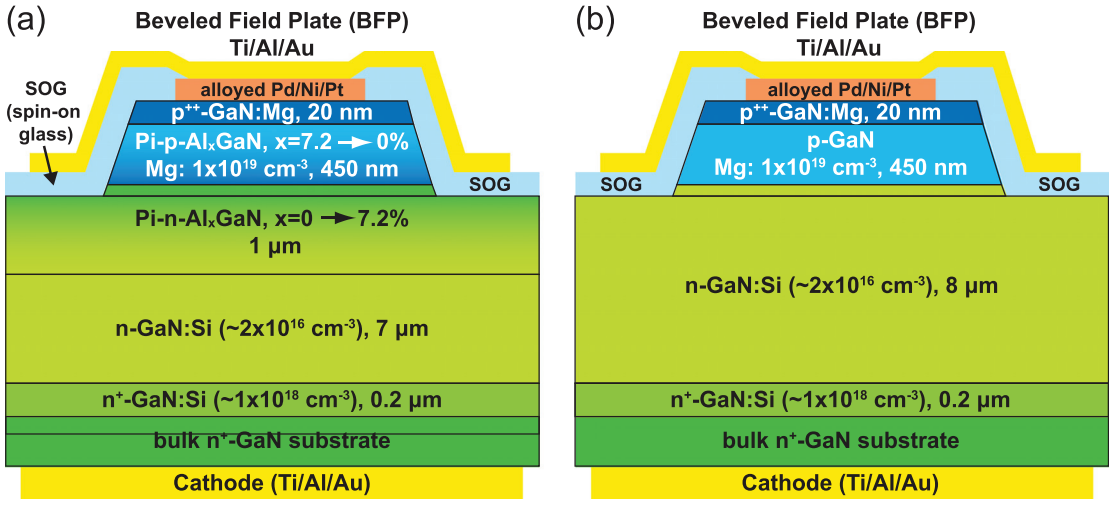

FIG. 1. Schematic layer structures and device cross sections of the (a) polarization-doped and (b) impurity-doped GaN p–n diodes.

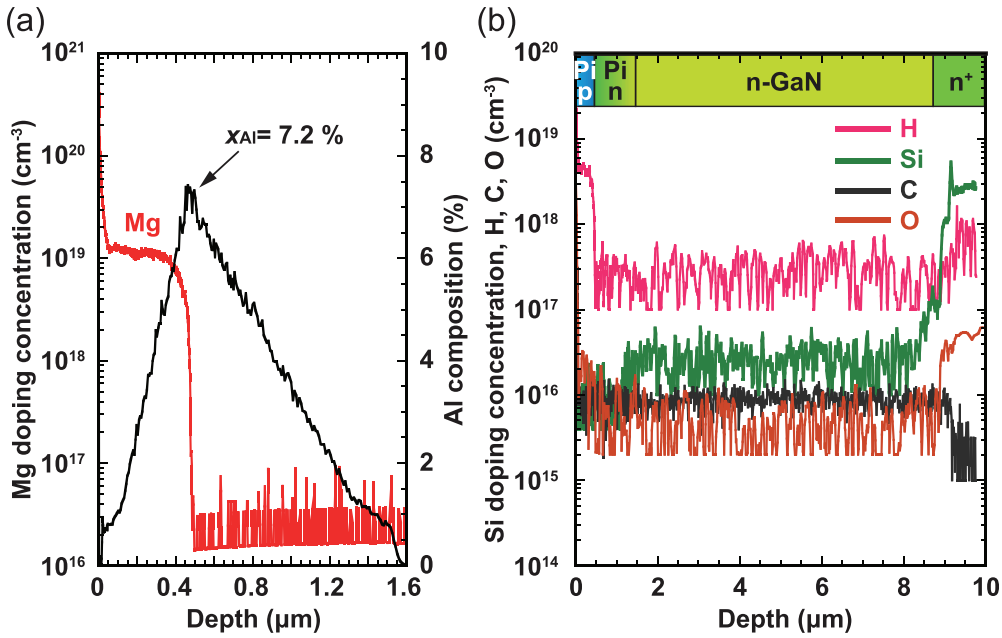

FIG. 2. SIMS analysis of the Pi-doped p–n diode sample. (a) Profiles of Mg doping and graded Al composition in the Pi-doped layers. (b) Si doping concentration and H, C, and O levels in the epitaxial layers.

temperature directly leads to a reduced compensation evidenced by the extracted net doping concentration (N_D-N_A) in the Si-doped drift layer, as will be discussed later.

In order to assess the effectiveness of the Pi-doping in the p-layer, Hall effect measurements were performed on both Pi-doped and impurity-doped samples and compared. The measurements were carried out on lithographically defined van der Pauw structures, with the p^{++} capping layer removed outside of the contact area. Table I shows the measured hole density and hole Hall mobility at room temperature (296 K). The Pi-doped p-layer shows a higher hole concentration ($1.6 \times 10^{17}\,cm^{-3}$) in comparison with the impurity-doped p-layer ($7.1 \times 10^{16}\,cm^{-3}$). Considering the same Mg-doping concentration in the two samples and assuming similar levels of compensation and H-passivation, the increased hole concentration ($8.9 \times 10^{16}\,cm^{-3}$) can be attributed to the Pi-doping. The expected polarization charge density (N_{pi}) can be calculated from the measured Al atomic concentration (x_{Al}) profile using[7,44]

$$N_{pi} = -5.22 \times 10^{13} \times \frac{\partial x_{Al}}{\partial z}\ cm^{-3}, \quad (1)$$

where z in cm is the depth from the sample surface. Equation 1 is valid only when $x_{Al} < 0.2$ and under the condition that the film is coherently strained. From Eq. (1), the average polarization charge density in the p-layer is $-8.4 \times 10^{16}\,cm^{-3}$. The magnitude of the distributed polarization charge is very close to the increase in the hole concentration. The agreement suggests that the graded $Al_{0.072}GaN$ layers are most likely coherently strained. To confirm this, x-ray diffraction reciprocal space mapping (RSM) is performed on the Pi-doped sample. Figure 3 shows the RSM of the asymmetric (105) reflection. It can be seen that the Pi-doped graded AlGaN layers are coherently strained to GaN. A slightly lower hole Hall mobility in the Pi-doped p-layer ($17.1\,cm^2/V\,s$) is observed relative to that in the impurity-doped p-layer ($23.2\,cm^2/V\,s$), likely due to the presence of alloy scattering.

To measure the net doping concentration in the n-drift region, capacitance–voltage (C–V) measurements were performed on diodes with 407-μm diameter at 100 kHz on both samples. To minimize parasitic capacitance at the device edge, large diodes with 407-μm in diameter without the field plate were measured. No frequency dispersion was observed between 10 kHz and 1 MHz. This is due to the insensitivity to depletion edge effects in the p^+-n^- junctions, where the hole concentration in the p^+-layer is much higher than the electron concentration in the n-layer.[11] Figure 4 shows the extracted N_D-N_A profile in the Pi-doped sample, as well as the polarization charge profile as

TABLE I. Hall effect measurement results on the p-layers at room temperature (296 K). Also shown is the hole concentration difference between the Pi-doped and impurity-doped samples as well as the calculated polarization charge density in the Pi-doped p-layer from the SIMS results.

	Sheet density (cm^{-2})	Hall mobility ($cm^2/V\,s$)	P-layer thickness (nm)	Bulk concentration (cm^{-3})
Impurity-doped	$+3.2 \times 10^{12}$	23.2	450	$+7.1 \times 10^{16}$
Pi-doped	$+7.2 \times 10^{12}$	17.1	450	$+1.6 \times 10^{17}$
Difference	$+4.0 \times 10^{12}$	N/A	N/A	$+8.9 \times 10^{16}$
Calculated polarization charge (SIMS)	-3.8×10^{12}	N/A	450	-8.4×10^{16}

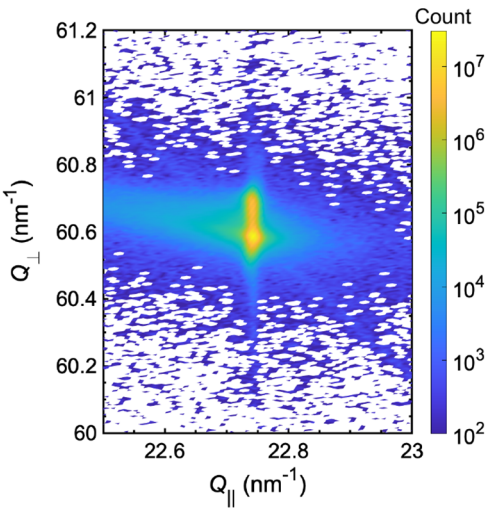

FIG. 3. X-ray diffraction reciprocal space mapping (RSM) of the asymmetric (105) reflections of the Pi-doped sample. The identical in-plane lattice constant confirms that the Pi-doped graded AlGaN layers are coherently strained to GaN.

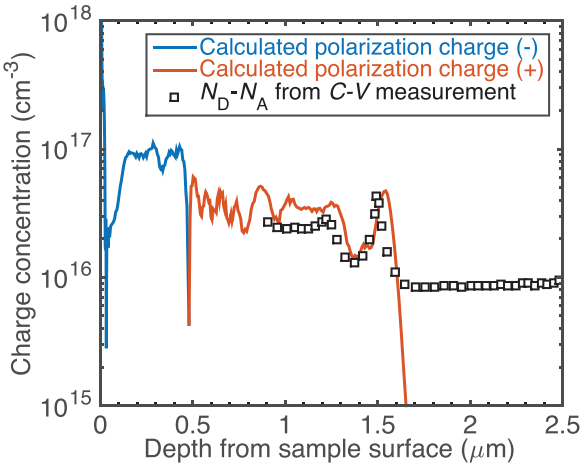

FIG. 4. Extracted net doping concentration (N_D-N_A) profile from capacitance–voltage (C–V) measurements on the Pi-doped sample and the calculated polarization charge profile from the SIMS measurement. A dielectric constant of 10.4 ε_0 for GaN was used in the C–V analysis and throughout this study.

calculated from Eq. (1). The slight deviation from an ideal linear $x_{Al}(z)$ profile leads to distinct features in the N_{pi} profile, with the most prominent peak located near 1.5 μm below the sample surface. Within the Pi-doped n-layer, the extracted N_D-N_A profile closely follows the N_{pi} profile, suggesting that polarization charge is indeed present. The average value of N_D-N_A is 2.5×10^{16} cm^{-3} in the Pi-doped n-layer. This number is slightly lower than the average N_{pi} value of 3.8×10^{16} cm^{-3}, likely due to point defect compensation. The N_D-N_A in the lower Si-doped n-layer is 8.6×10^{15} cm^{-3}. This value is found to be higher than that in the impurity-doped sample, which shows an average N_D-N_A of $\sim 2 \times 10^{15}$ cm^{-3}. Since the target Si-doping concentration is the same in these two samples, the difference in N_D-N_A is ascribed to different compensation levels due to slightly different growth conditions. As mentioned earlier, the entire n-drift layer of the Pi-doped sample was grown at a slightly hotter temperature, leading to a lower level of carbon incorporation. Because of the difference in N_D-N_A, one needs to compare the electric-field distribution between the two types of devices instead of a direct comparison of their breakdown voltages, as detailed later.

Figure 5 shows the forward I-V characteristics of both the Pi-doped and impurity-doped p–n diodes. The diodes all show textbook-like near-ideal turn-on behavior: a Shockley–Read–Hall (SRH)-recombination-dominated region below ~2.6 V with an ideality factor of ~2.0, followed by a diffusion-dominated region with near-unity ideality factor (~1.1 in the Pi-doped diode). Detailed

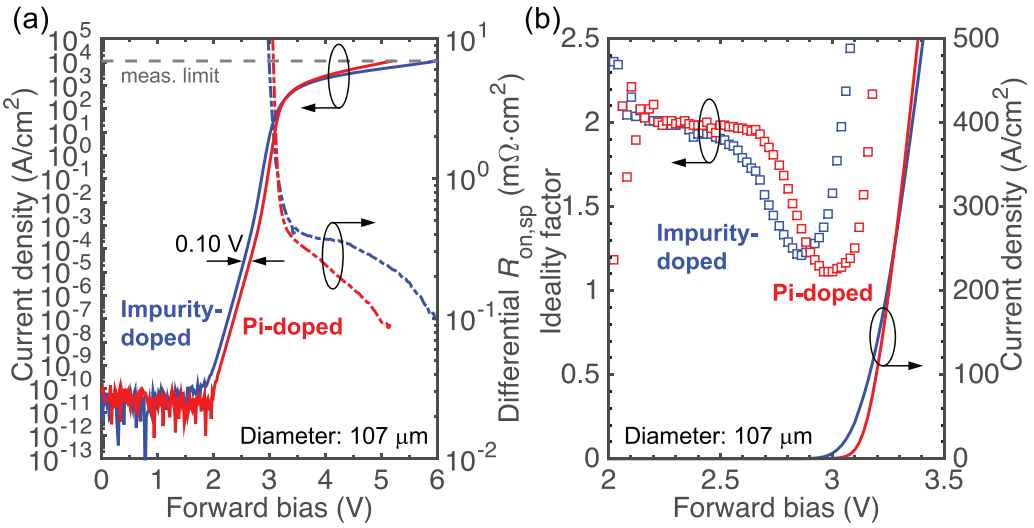

FIG. 5. Forward I–V characteristics of the Pi-doped p–n diode in comparison with the impurity-doped p–n diode.

analysis of the turn-on behavior in the same impurity-doped diode has been reported in Ref. 17, so will not be repeated here. Notably, the turn-on voltage of the Pi-doped p–n diode is 0.10 V higher. This has been confirmed on all measured devices with no size-dependence. Such a difference can be primarily attributed to the increase in the bandgap in the Pi-doped p–n junction, where a maximum bandgap increase in 0.13 eV is expected at the junction edge.[45] This value is similar with the measured increase in the turn-on voltage. The differential specific on-resistance ($R_{on,sp}$) after turn-on for both types of diodes is below 0.4 mΩ cm^2 and shows a decrease with the increase in forward bias. The Pi-doped diode exhibits lower differential $R_{on,sp}$ at the same forward bias, likely due to the higher average net doping concentration in the n-drift region. At 11 kA/cm^2 (the current compliance during measurements), the differential $R_{on,sp}$ reaches ~0.1 mΩ cm^2 in both diodes. The nonlinearity of the I–V characteristics and the corresponding decrease in differential $R_{on,sp}$ after the full turn-on of the diodes are likely caused by a combination of multiple effects, including non-linearity of the p-Ohmic contacts, conduction modulation due to hole injection into the drift layers, and photo-recycling effects.[46]

Figure 6 shows the temperature-dependent reverse I–V characteristics of the Pi-doped p–n diode. The extracted breakdown voltage (defined at 1 A/cm^2) increases with the increase in temperature. This is a signature of avalanche breakdown and is highly desirable in practical power devices. The increase in avalanche breakdown voltage with the increase in temperature is due to the increase in the phonon scattering rate, which leads to a reduction of the impact-ionization coefficients. Similar breakdown behaviors were observed in our previous generation of the Pi-doped p–n diodes in which avalanche breakdown was confirmed with the assistance of optical excitations.[40,41] A high room-temperature BV of 1252 V is achieved, thanks to the low net doping density in the Pi-doped n-layer, which allows for the spreading of the electric-field across the whole drift layer. Together with the low $R_{on,sp}$ of 0.1 mΩ cm^2, the high avalanche BV in the Pi-doped p–n diode results in a Baliga's figure-of-merit ($BV^2/R_{on,sp}$) of 15.7 GW/cm^2, similar with state-of-the-art impurity-doped GaN p–n diodes.[14–23]

The impurity-doped p–n diodes [Fig. 1(b)] also show avalanche breakdown, as reported in our previous work.[17]

The electric-field profile in the 8-μm-thick n-drift layer is calculated at BV for both samples by solving Poisson's equation in one-dimension, as shown in Fig. 7. The net doping profiles are simplified based on the actual profile extracted from C–V measurements. Since both the p-layer above and the n$^+$ buffer layer underneath the n-drift layer are much more heavily doped compared with the n-drift layer, their depletion widths are much smaller than the n-drift layer thickness that can be neglected in the calculations. It is clear that both samples feature a fully depleted n-drift layer at BV due to the punch-through (PT) design. At the metallurgical junction interface, the apparent breakdown electric field in the Pi-doped diode is calculated to be 2.43 MV/cm. On the other hand, the impurity-doped diode has a lower apparent breakdown electric field of 1.92 MV/cm despite a higher room-temperature avalanche BV of 1406 V.[17] This is largely due to the lower N_D-N_A in the n-layer of the impurity-doped diode, as shown in Fig. 7. Due to the difference in N_D-N_A, neither the apparent breakdown electric field nor the breakdown voltage is directly comparable between the two samples, as the breakdown field is known to increase with the increase in N_D-N_A,[47] while the BV depends on both the N_D-N_A profile and the drift layer thickness. It is also difficult to benchmark the extracted apparent breakdown electric fields against the near-ideal breakdown electric field of GaN as a function of net doping concentration recently established in Ref. 47, since the breakdown electric field is defined under non-punch-through (NPT) conditions while both of our diode samples are of PT design.

It should be noted that the apparent breakdown fields based on the 1D modeling in both samples are expected to be higher with better edge termination, since the presence of electric-field crowding is still expected at the device edge with our unoptimized field-plate design. Due to the larger bandgap of AlGaN at the junction edge, a larger breakdown field is expected in Pi-doped p–n diodes compared with the ideal GaN values. This is another advantage of Pi-doped p–n junctions based on graded AlGaN. To verify this experimentally in the

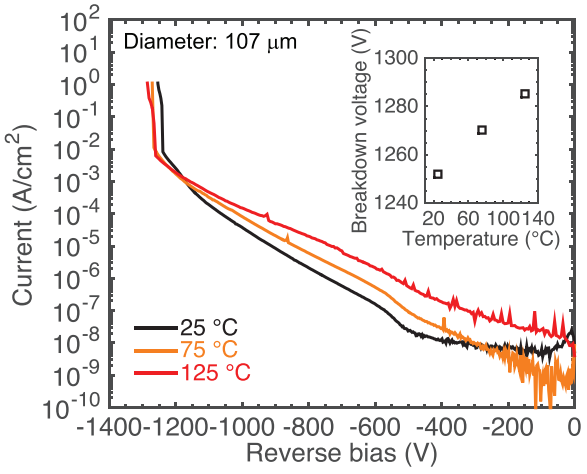

FIG. 6. Reverse I–V characteristics of the Pi-doped GaN p–n diode under different temperatures, confirming avalanche. Inset: extracted breakdown voltage at 1 A/cm^2 vs temperature. The impurity p–n diodes also show robust avalanche as reported in our earlier work,[17] so not shown here.

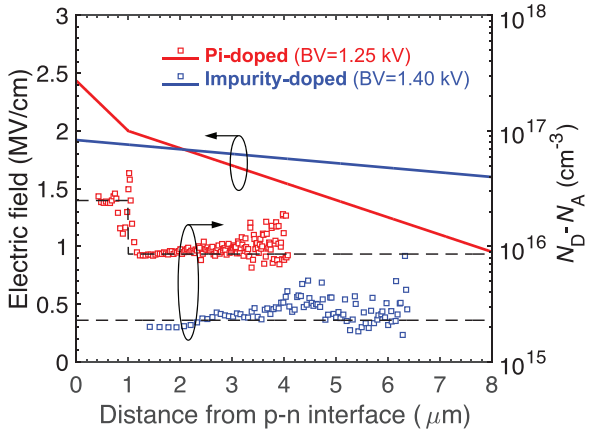

FIG. 7. Calculated 1D electric-field profile at the breakdown voltage in the Pi-doped and impurity-doped p–n diodes. The apparent charge profile extracted from C–V measurements (squares) and the simplified models (dashed lines) used for the electric-field calculation are also shown.

future, the net doping profile in the drift layer of the impurity-doped diode as a control should be made identical with the Pi-doped diode.

In conclusion, near-ideal forward and reverse *I-V* characteristics were demonstrated in polarization-doped GaN p–n diodes employing AlGaN layers with a linearly graded Al composition between 0 and 7.2%. Pi-doping through coherently strained AlGaN was confirmed by two signatures: (i) an expected increase in hole concentration ($8.9 \times 10^{16}\,cm^{-3}$) in the Pi-doped p-layer was observed from Hall effect measurements, and the measured value agrees well with the expected value; (ii) a measured N_D-N_A profile from *C-V* measurements in the Pi-doped n-layer shows excellent agreement with the expected polarization charge profile. The Pi-doped p–n diode exhibits a high avalanche breakdown voltage of ~1.25 kV, thanks to the record-low net doping concentration of $2.5 \times 10^{16}\,cm^{-3}$ in the Pi-doped n-layer. A decent apparent breakdown electric field of 2.43 MV/cm is extracted despite the non-ideal edge termination. The near-ideal junction behaviors serve as solid proof that Pi-bulk doping is feasible to be incorporated in GaN devices. The benefit of increased hole concentration from Pi-doping has been confirmed, while other projected advantages, such as the reduction of temperature and frequency dispersion, require further investigations. This demonstration together with the demonstration of laser diodes with the shortest wavelength of 271.8 nm by Zhang *et al.*[48] indicates that distributed polarization doping available in AlGaN presents some uniquely competitive advantages in comparison with other wide bandgap semiconductors.

This work was supported in part by the ARPA-E SWITCHES Program (No. DE-AR0000454) monitored by Tim Heidel and Isik Kizilyalli, in part by AFOSR under Grant No. FA9550-17-1-0048 monitored by Ken Goretta, and carried out at the Cornell Nanoscale Science and Technology Facilities (CNF) sponsored by the NSF under No. NNCI-202523.

AUTHOR DECLARATIONS

Conflict of Interest

The authors have no conflicts to disclose.

Author Contributions

K.N. and W.L. contributed equally to this work.

DATA AVAILABILITY

The data that support the findings of this study are available within this article.

REFERENCES

[1]U. K. Mishra, L. Shen, T. E. Kazior, and Y. F. Wu, Proc. IEEE **96**, 287 (2008).
[2]Y. Yue, Z. Hu, J. Guo, B. S. Rodriguez, G. Li, R. Wang, F. Faria, T. Fang, B. Song, X. Gao, S. Guo, T. Kosel, G. Snider, P. Fay, D. Jena, and H. Xing, IEEE Electron Devices Lett. **33**, 988 (2012).
[3]K. Shinohara, D. Regan, A. Corrion, D. Brown, Y. Tang, J. Wong, G. Candia, A. Schmitz, H. Fung, S. Kim, and M. Micovic, in *IEEE International Electron Devices Meeting (IEDM)* (IEEE, 2012), pp. 27–22.
[4]M. Zhu, B. Song, M. Qi, Z. Hu, K. Nomoto, X. Yan, Y. Cao, W. Johnson, E. Kohn, D. Jena, S. Member, H. G. Xing, and S. Member, IEEE Electron Devices Lett. **36**, 375 (2015).
[5]L. Nela, J. Ma, C. Erine, P. Xiang, T.-H. Shen, V. Tileli, T. Wang, K. Cheng, and E. Matioli, Nat. Electron. **4**, 284 (2021).
[6]K. J. Chen, O. Häberlen, A. Lidow, C. L. Tsai, T. Ueda, Y. Uemoto, and Y. Wu, IEEE Trans. Electron Devices **64**, 779 (2017).
[7]O. Ambacher, B. Foutz, J. Smart, J. R. Shealy, N. G. Weimann, K. Chu, M. Murphy, A. J. Sierakowski, W. J. Schaff, L. F. Eastman, R. Dimitrov, A. Mitchell, and M. Stutzmann, J. Appl. Phys. **87**, 334 (2000).
[8]R. Chaudhuri, S. J. Bader, Z. Chen, D. A. Muller, H. G. Xing, and D. Jena, Science **365**, 1454 (2019).
[9]D. Jena, S. Heikman, D. Green, D. Buttari, R. Coffie, H. Xing, S. Keller, S. DenBaars, J. S. Speck, U. K. Mishra, and I. Smorchkova, Appl. Phys. Lett. **81**, 4395 (2002).
[10]J. Simon, V. Protasenko, C. Lian, H. Xing, and D. Jena, Science **327**, 60 (2010).
[11]P. Kozodoy, S. P. DenBaars, and U. K. Mishra, J. Appl. Phys. **87**, 770 (2000).
[12]W. Shockley and W. T. Read, Phys. Rev. **87**, 835 (1952).
[13]S. M. Sze and K. K. Ng, *Physics of Semiconductor Devices* (John Wiley & Sons, New Jersey, 2006), p. 519.
[14]I. C. Kizilyalli, A. P. Edwards, H. Nie, D. Disney, and D. Bour, IEEE Trans. Electron Devices **60**, 3067 (2013).
[15]K. Nomoto, Z. Hu, B. Song, M. Zhu, M. Qi, R. Yan, V. Protasenko, E. Imhoff, J. Kuo, N. Kaneda, T. Mishima, T. Nakamura, D. Jena, and H. G. Xing, in *IEEE International Electron Devices Meeting (IEDM)* (IEEE, 2015).
[16]K. Nomoto, B. Song, Z. Hu, M. Zhu, M. Qi, N. Kaneda, T. Mishima, T. Nakamura, D. Jena, and H. G. Xing, IEEE Electron Device Lett. **37**, 161 (2016).
[17]Z. Hu, K. Nomoto, B. Song, M. Zhu, M. Qi, M. Pan, X. Gao, V. Protasenko, D. Jena, and H. Xing, Appl. Phys. Lett. **107**, 243501 (2015).
[18]A. M. Armstrong, A. A. Allerman, A. J. Fischer, M. P. King, M. S. Van Heukelom, M. W. Moseley, R. J. Kaplar, J. J. Wierer, M. H. Crawford, and J. R. Dickerson, Electron. Lett. **52**, 1170 (2016).
[19]J. Wang, L. Cao, J. Xie, E. Beam, R. McCarthy, C. Youtsey, and P. Fay, Appl. Phys. Lett. **113**, 023502 (2018).
[20]H. Fu, K. Fu, S. R. Alugubelli, C.-Y. Cheng, X. Huang, H. Chen, T.-H. Yang, C. Yang, J. Zhou, J. Montes, X. Deng, X. Qi, S. M. Goodnick, F. A. Ponce, and Y. Zhao, IEEE Electron Device Lett. **41**, 127 (2020).
[21]H. Ohta, N. Asai, F. Horikiri, Y. Narita, T. Yoshida, and T. Mishima, IEEE Electron Device Lett. **41**, 123 (2020).
[22]K. W. Nie, W. Z. Xu, F. F. Ren, D. Zhou, D. F. Pan, J. D. Ye, D. J. Chen, R. Zhang, Y. D. Zheng, and H. Lu, IEEE Electron Device Lett. **41**, 469 (2020).
[23]Z. Bian, K. Zeng, and S. Chowdhury, IEEE Electron Device Lett. (on line 2022).
[24]T. Maeda, T. Narita, H. Ueda, M. Kanechika, T. Uesugi, T. Kachi, T. Kimoto, M. Horita, and J. Suda, in IEEE International Electron Devices Meeting (IEDM) (2018).
[25]H. Fukushima, S. Usami, M. Ogura, Y. Ando, A. Tanaka, M. Deki, M. Kushimoto, S. Nitta, Y. Honda, and H. Amano, Jpn. J. Appl. Phys., Part 1 **58**, SCCD25 (2019).
[26]T. Oka, T. Ina, Y. Ueno, and J. Nishii, Appl. Phys. Express **8**, 054101 (2015).
[27]H. Nie, Q. Diduck, B. Alvarez, A. P. Edwards, B. M. Kayes, M. Zhang, G. Ye, T. Prunty, D. Bour, and I. C. Kizilyalli, IEEE Electron Device Lett. **35**, 939 (2014).
[28]D. Shibata, R. Kajitani, M. Ogawa, K. Tanaka, S. Tamura, T. Hatsuda, M. Ishida, and T. Ueda, in Technical Digest-IEEE International Electron Devices Meeting (IEDM) (IEEE, 2016), pp. 10–1.
[29]D. Ji, C. Gupta, S. H. Chan, A. Agarwal, W. Li, S. Keller, U. K. Mishra, and S. Chowdhury, in IEEE International Electron Devices Meeting (IEDM) (IEEE, 2017), pp. 9–4.
[30]Y. Zhang, M. Sun, D. Piedra, J. Hu, Z. Liu, Y. Lin, X. Gao, K. Shepard, and T. Palacios, in IEEE International Electron Devices Meeting (IEDM) (IEEE, 2017), pp. 9–2.
[31]W. Li, K. Nomoto, K. Lee, S. M. Islam, Z. Hu, M. Zhu, X. Gao, M. Pilla, D. Jena, and H. G. Xing, IEEE Trans. Electron Devices **65**, 2558 (2018).
[32]W. Li, K. Nomoto, K. Lee, S. M. Islam, Z. Hu, M. Zhu, X. Gao, J. Xie, M. Pilla, D. Jena, and H. G. Xing, Appl. Phys. Lett. **113**, 062105 (2018).
[33]T. Narita, K. Tomita, S. Yamada, and T. Kachi, Appl. Phys. Express **12**, 011006 (2019).
[34]H. G. Xing, B. Song, M. Zhu, Z. Hu, M. Qi, K. Nomoto, and D. Jena, in Proceedings 73rd Annual Device Research Conference (DRC) (IEEE, 2015), p. 51.
[35]W. Li, K. Nomoto, A. Sundar, K. Lee, M. Zhu, Z. Hu, E. Beam, J. Xie, M. Pilla, X. Gao, S. Rouvimov, D. Jena, and H. G. Xing, Jpn. J. Appl. Phys., Part 1 **58**, SCCD15 (2019).

[36]W. Li, M. Zhu, K. Nomoto, Z. Hu, X. Gao, M. Pilla, D. Jena, and H. G. Xing, in 31st International Symposium on Power Semiconductor Devices and ICs (ISPSD) (IEEE, 2018), p. 228.
[37]S. Li, M. Ware, J. Wu, P. Minor, Z. Wang, Z. Wu, Y. Jiang, and G. J. Salamo, Appl. Phys. Lett. **101**, 122103 (2012).
[38]Y. Enatsu, C. Gupta, S. Keller, S. Nakamura, and U. K. Mishra, Semicond. Sci. Technol. **32**, 105013 (2017).
[39]M. Qi, K. Nomoto, M. Zhu, Z. Hu, Y. Zhao, B. Song, G. Li, P. Fay, H. Xing, and D. Jena, in *73rd Annual Device Research Conference (DRC)* (IEEE, 2015), p. 31.
[40]C. De Santi, E. Fabris, K. Nomoto, Z. Hu, W. Li, X. Gao, D. Jena, H. G. Xing, G. Meneghesso, M. Meneghini, and E. Zanoni, in *IEEE International Electron Devices Meeting (IEDM)* (IEEE, 2018), pp. 30–32.
[41]E. Fabris, C. De Santi, A. Caria, K. Nomoto, Z. Hu, W. Li, X. Gao, D. Jena, H. G. Xing, G. Meneghesso, E. Zanoni, and M. Meneghini, IEEE Trans. Electron Devices **66**, 4597 (2019).
[42]M. Zhu, M. Qi, K. Nomoto, Z. Hu, B. Song, M. Pan, X. Gao, D. Jena, and H. G. Xing, Appl. Phys. Lett. **110**, 182102 (2017).
[43]Z. Hu, K. Nomoto, M. Qi, W. Li, M. Zhu, X. Gao, D. Jena, and H. G. Xing, IEEE Electron Device Lett. **38**, 1071 (2017).
[44]Y. Cao, R. Chu, R. Li, M. Chen, and A. J. Williams, Appl. Phys. Lett. **108**, 112101 (2016).
[45]F. Yun, M. A. Reshchikov, L. He, T. King, H. Morkoç, S. W. Novak, and L. Wei, J. Appl. Phys. **92**, 4837 (2002).
[46]S. Han, S. Yang, Y. Li, Y. Liu, and K. Sheng, in *31st International Symposium on Power Semiconductor Devices and ICs (ISPSD)* (IEEE, 2019), p. 63.
[47]T. Maeda, T. Narita, S. Yamada, T. Kachi, T. Kimoto, M. Horita, and J. Suda, IEEE Electron Device Lett. **43**, 96 (2022).
[48]Z. Zhang, M. Kushimoto, T. Sakai, N. Sugiyama, L. Schowalter, C. Sasaoka, and H. Amano, Appl. Phys. Express **12**, 124003 (2019).